International Journal of Heat and Fluid Flow 108 (2024) 109486

Contents lists available at ScienceDirect

International Journal of Heat and Fluid Flow

journal homepage: www.elsevier.com/locate/ijhff

Large scale structures modification of a spatially evolving turbulent boundary layer grazing over circular cavities

Francesco Scarano [a,b,*], Marc C. Jacob [b], Erwin R. Gowree [a]

[a] Département Aérodynamique et Propulsion (DAEP) ISAE-SUPAERO, Université de Toulouse, 10, avenue Edouard Belin 31400, Toulouse, France

[b] Laboratoire de Mécanique des Fluides et d'Acoustique, Ecole Centrale de Lyon; Institut National des Sciences Appliquées Lyon; Université Claude Bernard Lyon I; Centre National de Recherche Scientifique, Université de Lyon, 36 av. Guy de Collongue F-69134 Ecully, France

ARTICLE INFO

Keywords:
Circular cavities
Uniform momentum zones
Turbulent boundary layer
Passive flow control

ABSTRACT

Two experimental investigations were conducted to characterise the impact of circular cavities on the streamwise development of a turbulent boundary layer. Hot-wire anemometry was employed to measure the boundary layer at different streamwise locations along a perforated surface. While the modification of the boundary layer thickness was negligible, the shape factor increased and the friction coefficient decreased with respect to the smooth baseline case. The skin friction downstream of the perforations was investigated by oil droplet interferometry, confirming the skin friction reduction reported in previous investigations. The contour of the premultiplied energy spectrogram showed a "two-peaks" behaviour, where the inner peak shifted towards lower wavelengths, λ_X^+, and upwards, suggesting that the streaks were shortened and lifted up by the cavities in the perforated region. The outer peak, can be associated with the enhancement of turbulent mixing and inner/outer layer interaction. Particle image velocimetry measurements, conducted in a streamwise plane downstream of the cavities, showed an increased Reynolds shear stress associated with a significant enhancement of the ejections contribution. A negligible variation in the number of Uniform Momentum Zones in the presence of cavities was observed, but a reduction in the modal velocity associated with the logarithmic region would confirm the formation of low momentum pathways. These outer structures play a significant role in the turbulent mixing enhancement that could be exploited for heat transfer purposes.

1. Introduction

Turbulent skin friction reduction or, more broadly, turbulent boundary layer control has been a subject of major scrutiny as wall bounded flows are predominantly turbulent in most engineering applications. A first approach consists of introducing a passive or active system that interacts with the small scales turbulence and interferes with the near wall cycle. This approach applies to riblets (Garcia-Mayoral and Jimenez, 2011) and spanwise wall oscillations (Jung et al., 1992) and recently by sinusoidal riblets (Cafiero and Iuso, 2022). However, the important role of the logarithmic eddies on turbulent skin friction, especially at high Reynolds numbers, $Re_\tau > 4000$, where $Re_\tau = U_\tau \delta/\nu$ and, U_τ, the friction velocity, δ, the boundary layer thickness and ν the kinematic viscosity, and conversely the decreasing importance of the near wall cycle even at moderate Reynolds number (Hwang, 2013), has been recently addressed and must therefore be accounted in turbulent boundary layer control strategies (de Giovanetti et al., 2016). At high Reynolds number the near wall cycle is found to be directly influenced by the outer large-scale structures, namely the hairpins (Gomit et al., 2018; Mathis et al., 2009). Modifying the large coherent structures is in return expected to have an effect on the near wall turbulence and on the skin friction as demonstrated experimentally by Duvvuri and McKeon (2016) and Deshpande et al. (2023). In addition, implementing a surface feature that interacts with large scale structures could be very beneficial, even at moderate Reynolds numbers, for heat transfer purposes by modifying the momentum exchange in the turbulent boundary layer.

Large eddy break-up devices (LEBUs) addressed turbulent skin friction reduction by suppressing large scale structures, inhibiting wall-normal fluctuations and adding small-scale turbulence. Despite promising results, recent investigations (Alfredsson and Örlü, 2018) evidenced that no overall drag benefit can be obtained with such techniques but suggested the application of LEBUs for heat transfer enhancement.

Among the techniques that modifies the outer scales, uniform blowing has proven to be effective in reducing turbulent skin friction drag, as demonstrated in both numerical simulations (Kametani et al.,

* Corresponding author.
E-mail address: fr.scarano@gmail.com (F. Scarano).

https://doi.org/10.1016/j.ijheatfluidflow.2024.109486
Received 12 October 2023; Received in revised form 26 May 2024; Accepted 21 June 2024
Available online 3 July 2024

2015) and experimental studies (Kornilov, 2015; Hwang and Biesiadny, 1997). A wall normal blowing, with a magnitude of approximately 0.1% of the free-stream velocity, enhances the wall-normal convection (Fukagata et al., 2002) and the energy in the outer scales. At the same time the uniform blowing increases the Reynolds shear stress and promotes the formation of an outer peak in the normal shear stress. An increase of the ejection frequency and intensity in the buffer layer is documented which is correlated with a wall shear stress reduction (Kornilov, 2015).

Perforated and dimpled surfaces as a potential technique to reduce the turbulent skin friction has been a topic of interest in the last decades. Due to the size of dimples (diameters of the order of δ) and cavities (diameter approximately 100–300 viscous units) it is expected that these surfaces interact with outer and logarithmic scales. Dimples were originally intended for heat transfer enhancement, but some authors reported promising results on skin friction and total drag reduction (Tay et al., 2015; van Nesselrooij et al., 2016). However, the inefficacy of dimples in reducing the total drag has been recently demonstrated by Spalart et al. (2019) and van Campenhout et al. (2023) using force balance measurements and large eddy simulations. This is thought to be due to an increase in the pressure drag contribution that completely overcomes the skin friction drag benefit. Silvestri et al. (2017), Gowree et al. (2019) and Severino et al. (2022) explored the application of circular cavities as turbulent skin friction drag reduction technique, however the role of the geometrical parameters, such as the diameter and the spacing, was ambiguous. Scarano et al. (2023a) focused on perforated surfaces (cavities of cylindrical shape, sealed at the bottom) at moderate Reynolds numbers ($Re_\tau < 1100$) highlighting the importance of the open area ratio (OAR), defined as the ratio between the perforated area and remaining solid surface, as governing parameter both for the modification of the mean and fluctuating component of the flow and for the local skin friction. A skin friction reduction of up to 20% was achievable for the largest open area ratio (0.47). At least for the highest open area ratio ($\geq$0.32), the cavities promote the formation of an outer peak in the turbulence intensity and a "two-peaks" behaviour in the contours of the premultiplied energy spectrogram. This modification of the turbulent activity is believed to be associated with a momentum flux and the presence of an additional streamwise roller in the logarithmic region. This momentum flux is thought to be responsible for the non-negligible pressure drag measured experimentally for dimpled surfaces.

However, it is still of a fundamental importance to study the modification that the boundary layer undergoes when grazing over a perforated or dimpled surface. Despite the skin friction drag reduction being potentially offset by the increase in form drag, if a compromise between these two drag components is achieved, the resulting turbulence redistribution on such surfaces can be beneficial for heat transfer applications by limiting the drag penalty. In addition, studying how cavities influence the turbulent structures and skin friction can be a useful first order approximation for modelling the physics of more complicated surfaces such as acoustic liners, even in the portion where the turbulent boundary layer is adapting to the modified surface. Recent studies by Kim et al. (2020) evidenced stronger inner/outer layer interaction over porous surfaces associated with enhanced turbulent mixing and Jaiswal and Ganapathisubramani (2024) underlined that the effect of permeable wall can also be felt by large-scale structures, leading to the disappearance of the logarithmic mean velocity law.

A detailed characterisation of just the two-dimensional flow, as well as the streamwise development of the turbulent boundary layer over perforated cavities is lacking in the literature. In order to gain deeper insights into the modifications of the turbulent boundary layer grazing over cavities, a sufficiently large flow field diagnostics, for instance through Particle Image Velocimetry (PIV) could offer a better perspective on the behaviour of the large-scale structures. PIV measurements of the boundary layer over dimpled surface was conducted by van Nesselrooij et al. (2016), however the study lacked comprehensive details regarding the modifications of the large-scale structures. It is therefore difficult to extrapolate their findings to circular cavities, thus supporting the need for the current study.

The paper is divided as follows: Section 2 outlines the experimental setup and methods used in this study. In Section 3, the streamwise development of the boundary layer statistics and integral quantities from hot wire measurements, along the perforated surface are presented. While relying on PIV measurements, in Section 4 we provide quadrant analysis results for several perforated surfaces and in Section 5 we highlight the modifications of the uniform momentum zones in the presence of cavities. Finally, in Section 6, we concluded on the physical mechanisms entailing turbulent boundary layer grazing over circular cavities observed so far and made suggestions for future research.

2. Experimental setup

Two separate experimental campaigns were conducted in the low-speed, closed-loop wind tunnel of ISAE-SUPAERO. The test model is a 2.5 m long, 1.2 m wide, horizontally mounted flat plate equipped with an elliptic leading edge and a flap to ensure a close-to-zero pressure gradient (acceleration parameter less than 10^{-7} Patel, 1965). The boundary layer is tripped using a 780 μm diameter wire placed downstream of the flat plate leading edge.

The flat plate features a square insert, measuring $l = 400$ mm, positioned 1.1 m downstream of the leading edge. This insert is designed to accommodate panels with a variety of surface characteristics, ranging from smooth to perforated models. The panels are made of plexiglass in order to minimise heat transfer between the wall and the hot wire probe during near-wall measurements. A similar set-up has been utilised in previous studies (Scarano et al., 2022b,a, 2023a).

The streamwise development of the turbulent boundary layer along an entire perforated model was characterised at 20 m/s. Here, we will focus only on the OAR = 0.47, shown in Fig. 1(a) and will be compared with the smooth baseline case. Intermediate OAR cases have been treated in Scarano et al. (2023a), and based on the naming convention adopted there the current test sample corresponds to the d6L11 case. Along the perforated model the measurements are always taken on the smooth portion between two adjacent cavities.

Due to the limited streamwise extent of the perforated region and the high OAR, which imposes a strong surface modification, the flow is not expected to reach a full equilibrium state on the perforated surface. Antonia and Luxton (1971) prescribed a development length of $10 - 15\delta$ downstream of the perturbation to be adequate for the flow to establish equilibrium. However, according to Gul and Ganapathisubramani (2022) high order statistics are expected to take more than $5 - 10\delta$ to recover a full equilibrium state. Due to the development of an internal boundary layer, the deviations occur first close to the wall and then they extend to a larger wall-normal distance because of the internal boundary layer growth. Ismail et al. (2018) suggests that at least 40δ are needed for the statistics to fully recover after the step change from rough to smooth surface. The equilibrium profile is recovered quicker for the smooth to rough profiles compared to the rough to smooth case, where at $x/\delta \cong 14$ it start to approach to those of the upstream condition (Gul and Ganapathisubramani, 2022).

Several studies that investigated the effect of similar surface modifications at a comparable friction Reynolds number (Gowree et al., 2019; Scarano et al., 2022b; Silvestri et al., 2017; Severino et al., 2022; Cafiero and Iuso, 2022; Scarano et al., 2023b), used a similar extension of the insert, between 15 and 20δ. A demonstration of the modification of the turbulent boundary layer when subjected to surface modification both in terms of energy content and integral parameters, even in the non-equilibrium portion, is believed to be relevant in several industrial contexts. The lack of asymptotic conditions should not affect the relevance of the results, as it is often found in real-life applications, for instance in ablated turbine blades or drone wings, or the turbulent boundary layer developing in the turbo-fan engine

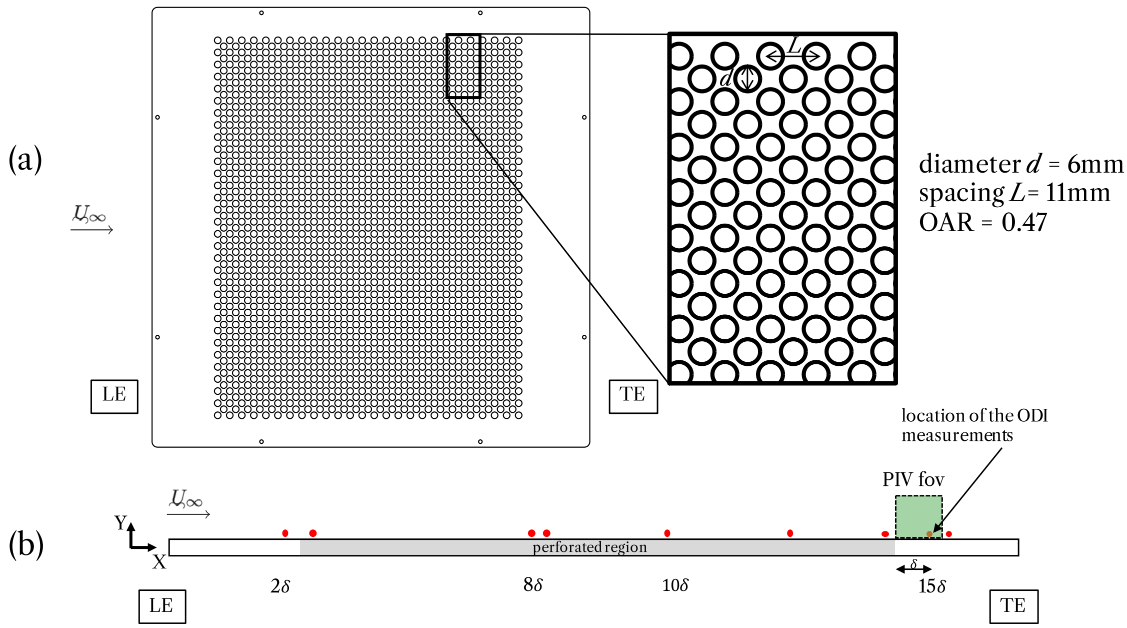

Fig. 1. Test model d6L11 used for the streamwise characterisation of the boundary layer (a) and measurements locations for the PIV and hot wire measurements along the centre-line of the model (red dots are the hot wire measurements for the streamwise characterisation) (b). (For interpretation of the references to colour in this figure legend, the reader is referred to the web version of this article.)

equipped with acoustic liners, where asymptotic conditions are unlikely to be reached.

A Dantec 55P15 boundary layer hot wire probe was employed, with a sampling frequency of 20 kHz. The wire was maintained at an operating temperature of roughly 230 °C, with the overheat ratio of 1.75. The 2D traversing system enables a minimum displacement in the direction normal to the wall (Y) of 12.5 μm, which falls within the range of 0.35 to 0.61 viscous lengths. The measurements are conducted at several streamwise locations illustrated in Fig. 1(b).

For direct skin friction evaluation of the perforated model, oil droplet interferometric (ODI) measurements were conducted on the d6L11 configuration and the smooth baseline case. The ODI is a simple alternative to the classic oil film interferometry (Naughton et al., 2003; Naughton and Sheplak, 2002) and it allows to infer the wall shear stress from the inter-fringe spacing variation in time. Further details of the technique can been found in Pailhas et al. (2009). The in-house code developed by Pailhas et al. (2009) has been used for the image processing. The measurements were performed on the same measurement location as the hot wire boundary layer surveys in Scarano et al. (2023a), approximately one boundary layer thickness downstream of the last row of cavities.

A second experimental campaign was conducted to complement the results reported by Scarano et al. (2023a) with stereoscopic particle image velocimetry. Several perforated models were tested with the open area ratio (OAR) ranging from 0.03 to 0.47 for three flow conditions: 10, 15 and 20 m/s (friction Reynolds number Re_τ of the baseline case ranging from 620 to 1090, boundary layer thickness, δ, around 20 mm). The reader should refer to Scarano et al. (2023a) for the models description and to Scarano et al. (2022a) for the baseline conditions. The measurement plane is positioned parallel to the flow in the (XY) plane. The PIV measurements are performed downstream of the perforated region along the centreline of the model to cover the region investigated in Scarano et al. (2023a) (see Fig. 1(b)). A Litron LDY 304 (527 nm) was used to illuminate the measurement region and it was shot from the top of the wind tunnel. The seeding was provided by a TOPAS olive oil atomiser located downstream of the diffuser of the tunnel. Image pairs were captured from the lateral perspective through the glass wall, employing a pair of MIRO LAB 340 cameras arranged in a stereoscopic configuration with a Scheimpflug angle of approximately 85°. Each camera has a resolution of 2560 × 1600 and is equipped with NIKON 300 mm f/4 lenses. For calibration, synchronisation and image acquisition, DANTEC DynamicStudio 6.4 is utilised. During each acquisition, 1000 statistically independent image pairs were acquired at 50 Hz. The samples were processed using DynamicStudio 6.4's 2D3C cross-correlation PIV algorithm. The size of the interrogation window is iteratively reduced from 64 × 64 pixels to 32 × 32 pixels with a 50% overlap. This results in a grid of 40 400 vectors within a field of view (FOV) of 65 mm × 45 mm. This FOV is then cropped to 45 mm × 45 mm, approximately $2\delta \times 2\delta$. Vectors near the wall are discarded due to reflections. Further details of the PIV setup can be found in Scarano et al. (2022a).

3. Streamwise development

The results reported in this section are a comparison between the d6L11 case (OAR = 0.47, see Scarano et al. (2023a) for details) and the smooth baseline case at 20 m/s.

3.1. Boundary layer quantities

The streamwise evolution of the boundary layer thickness is shown in Fig. 2. For the baseline case a mild increase in the boundary layer is observed when moving downstream and this is due to the boundary layer developing in the streamwise direction. The perforated case exhibits a similar increase: the small differences with respect to the baseline case are thought to be due to the uncertainty in the measurements calculated following (Titchener et al., 2015).

The streamwise evolution in the shape factor is reported in Fig. 3; for the baseline case the shape factor remains constant along the entire model (Fig. 3 (b)) and, for similar values of the momentum thickness based Reynolds number, Re_θ, a good match with the DNS from Schlatter and Orlu (2010) is recovered. For the perforated case, the shape factor increases with respect to the baseline starting from one third of the model (about 5δ downstream of the first cavity). The current results indicate that a perforated surface can promote a non-negligible increase in the shape factor, however the value of the shape factor for all the streamwise locations is nowhere near to that corresponding to flow separation. In the downstream part of the model, the shape factor

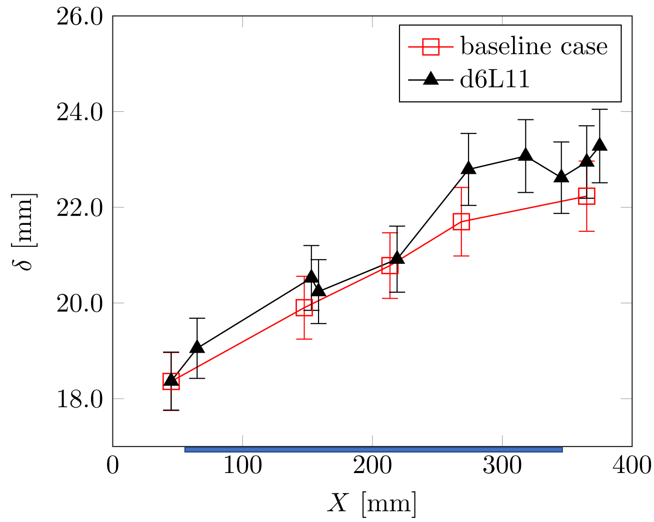

Fig. 2. Streamwise evolution of the boundary layer thickness, δ, at 20 m/s. In blue the perforated region is reported. (For interpretation of the references to colour in this figure legend, the reader is referred to the web version of this article.)

decreases and then gradually approaches the baseline case value that is expected to be recovered further downstream, along the smooth portion of the plate.

In Fig. 4 the Re_θ and the friction Reynolds number, Re_τ, for the d6L11 case are plotted against the Re_{θ_0} on the baseline case at the same streamwise location. The perforated wall (d6L11) promotes the increase in the momentum thickness based Reynolds number along the streamwise coordinate. A bump along the first portion of the perforated model in Fig. 4(a) may be associated with the boundary layer not being yet in equilibrium with the surface. A similar behaviour can be noted in Fig. 4(b): only above $Re_{\theta_0} \cong 3200$ (about 8δ downstream of the first row of cavities) the flow seems to start approaching an equilibrium along the perforated surface. For $Re_{\theta_0} > 3200$, the rate of increase of the friction Reynolds number Re_τ is similar with respect to the baseline case, but the curve is shifted downward whereas the two configurations do not follow the same trends below $Re_{\theta_0} \cong 3200$.

3.2. Diagnostic plot

To better underline the state of the turbulent boundary layer when developing over the cavities, the diagnostic plot is reported in Fig. 5. It can be noticed that the flow over the cavities cannot be considered as fully rough but rather transitionally rough. This is because the diagnostic plot is only slightly shifted with respect to the smooth baseline case value and the semi-empirical relation proposed by Alfredsson et al. (2011) and Castro et al. (2013) which is valid for smooth walls (solid line in the figure). Another possible explanation for this moderate shift could be due the decrease of the Reynolds number, Re_τ, with respect to the smooth baseline case, similar behaviour was reported by Castro et al. (2013), but their study was only limited to smooth surface. According to Gul and Ganapathisubramani (2022) for a smooth to rough step change, the diagnostic plot undershoot the smooth wall condition while in the current case the opposite trend can be identified except for the region where $U/U_\infty < 0.5$.

The diagnostic plots at different streamwise positions along the perforated model are also reported: increasing marker size represents further downstream positions as indicated by the arrow. The first profiles deviate from the smooth baseline condition while the profiles downstream of approximately 8δ start to collapse. This can suggest that, downstream 8δ, the flow starts to approach an equilibrium condition which however is not fully reached due to the limited streamwise extent of the domain.

3.3. Skin friction coefficient

The streamwise evolution of the friction coefficient is shown in Fig. 6. The baseline case, as well as the first measurement point on the smooth part upstream of the first row of cavities match very well the DNS results by Schlatter and Orlu (2010) and the Coles–Fernholtz relation that applies to smooth walls. This is a confirmation that, upstream of the perforations, the boundary layer has reached a developed turbulent state (Kametani et al., 2015).

The friction velocity has been obtained using the Clauser-like method proposed by Rodríguez-López et al. (2015) while using the Spalding equation as proposed by Kendall and Koochesfahani (2008). The method proposed by Rodríguez-López et al. (2015) is reported to work for adverse pressure gradient or distorted turbulent boundary layers. It allows a fit without choosing *a-priori* values of the constant κ and B. In the current case the constants are found not to vary with respect to the canonical boundary layer over the smooth surface. The fitting technique is used for all the measurements along the streamwise direction. The profiles taken on the first portion of the perforated region, where the flow is not in equilibrium with the perforated surface, exhibit only a short portion of logarithmic region. This leads to a larger fitting error with respect to the less-distorted profile encountered further downstream as depicted in Fig. 6 by the larger error-bars in the measurement along the first portion of the perforated surface. The direct skin friction measurements obtained with the ODI downstream of the perforated region are reported in green in Fig. 6 and are found to be within the uncertainty of the skin friction evaluation obtained using the fitting technique.

The friction coefficient drops right downstream of the first row of cavities until it reaches a plateau region at about $X \cong 170$ mm (about 8δ downstream of the first cavity). The sudden change in skin friction downstream the abrupt change from smooth to perforated surface can represent the formation of an internal boundary layer (Gul and Ganapathisubramani, 2022). The results show qualitative similarities with the boundary layer with uniform blowing by Kametani et al. (2015); this is surprising as already underlined by Scarano et al. (2023a) due to the different flow mechanisms involved in the presence of the cavities, despite increasing the inner/outer motion as it will be detailed hereafter, cannot promote a blowing mechanism. What can be underlined in the figure is that, in contrast with the results by Kametani et al. (2015), downstream of the perforated region, the friction coefficient does not recover the baseline condition immediately but remains almost constant over a streamwise extension of at least 3δ. The recovery distance of the skin friction downstream of the perforated plate could not be found due to limitations in the traversing and in the limited streamwise dimension of the test section.

3.4. Premultiplied energy spectra

For the d6L11 case at 20 m/s, the development of the outer energetic region in the streamwise direction can be observed in the contours of the premultiplied energy spectrograms shown in Fig. 7. The spectra are computed using the Welch algorithm with 98 segments, each employing a window size of 2^{11} samples and a 50% overlap. The non-dimensional premultiplied spectra are mapped along the wall, $Y^+ = YU_\tau/\nu$, and the reduced streamwise wavelength $\lambda_X^+ = \lambda_x U_\tau/\nu$, derived by applying Taylor's hypothesis and here the turbulence was considered frozen even on the perforated region. The actual friction velocity is used to normalise the spectra. Maps are plotted at the streamwise positions (I) to (VI) over the whole model along the mid-span, as shown in Fig. 7.

At the position (I) the contours of the premultiplied energy spectrogram inner peak exhibits a shift towards lower values of λ_X^+. This can be linked to the abrupt change in the boundary conditions at the leading cavities as it modifies the streamwise streaks coherence. Up to the position (IV) the spectrum shows a single broader region while λ_X^+ is slightly reduced compared to the baseline case but the centre

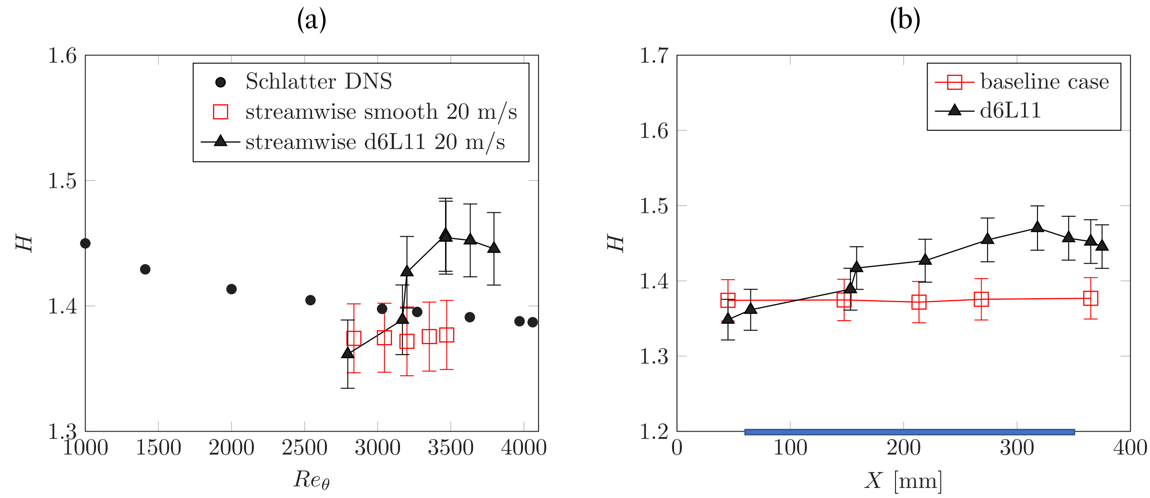

Fig. 3. Streamwise evolution of the boundary layer shape factor at 20 m/s, (a) evolution against the local Re_θ, (b) evolution along the model, in blue at the bottom the extension of the perforated region is reported. (For interpretation of the references to colour in this figure legend, the reader is referred to the web version of this article.)

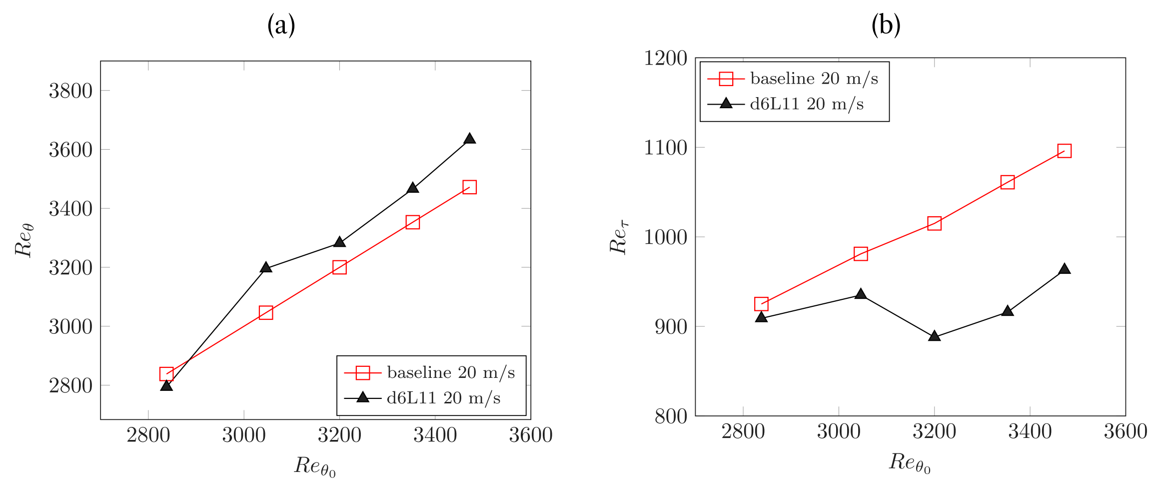

Fig. 4. Streamwise evolution of the (a) Re_θ, (b) Re_τ of d6L11 plotted against the Re_{θ_0} of the baseline surface at the same streamwise position along the perforated surface, 20 m/s.

of the hump is shifted upward. Downstream of the cavities (VI) the spectrum exhibits two peaks. The inner peak has similar Y^+ values but they are associated with a smaller wavelength, $\lambda_X^+ \cong 860$ compared to the inner peak of the smooth baseline. Moreover the smooth baseline case does not show any outer region that corresponds to $\lambda_X^+ \cong 1850$ as the perforated case does.

The peak position in the spectrum and the associated wavelength have been tracked along the streamwise direction, the results are shown in Fig. 8. The presence of the outer peak has been defined as a relative maximum in the 2D contour maps that have a value approximately equal to the inner peak. It can be noted that at the upstream edge of the perforated area, that is, at the front row of cavities, the cavities reduce considerably the wavelength of the peak. (Shahzad et al., 2023) performed pore-resolved numerical simulations over acoustic liners having a similar open area ratio of the current investigation. They evidenced a shortening of the streaks with respect to the smooth baseline case which was also reported in previous investigations on porous and permeable surfaces (Kuwata and Suga, 2016). According to Jaiswal and Ganapathisubramani (2024) permeable surfaces break-up the near wall structures reducing the near wall turbulent energy. Shahzad et al. (2023) showed the formation of a distinct additional energy peak in the spanwise velocity spectrogram at a wavelength equal to the orifice spacing. It is very interesting to underline that, looking at the Fig. 7(I), the inner peak wavelength scales with the distance between the cavities in wall units, $L^+ \cong 500$.

In addition, the inner peak location clearly moves towards higher values of Y^+ reaching the maximum of, $Y^+ \cong 45$, at the centre of the model. As reported by Jaiswal and Ganapathisubramani (2024) for porous surfaces, the increase in the "inner peak" Y^+ in the fore portion of the perforated plate can be attributed to a roughness sub-layer that pushes the energetic flow away from the surface. Further downstream, the inner peak normal-to-wall location approaches that of the baseline case. The inner peak wavelength starts to grow downstream of the perforations but without recovering the wavelength of the baseline case.

Manes et al. (2011) associated the increased mixing on porous foams to Kelvin–Helmholtz (KH) instabilities that occur at the interface of the porous surface up to $Y/\delta = 0.1$. However (Jaiswal and Ganapathisubramani, 2024) did not report KH instabilities in their investigation. In the current case, a sharp peak that could be associated with a KH-like instability is not discernible, however the wavelength is equal to the spacing between the cavities as reported by Shahzad et al. (2023), suggesting that the cavities drain energy from the near-wall cycle and rearrange it at a lengthscale that corresponds to the perforated pattern.

The formation of a secondary outer peak in the spectrum starting from approximately two thirds of the perforated region ($X \cong 270$ mm, $X/\delta \cong 12$, described in the figure by the dashed line) is very clear. The wavelength associated with this outer peak increases while approaching a value of about $\lambda_X^+ \cong 1850$. The outer peak wall-normal location

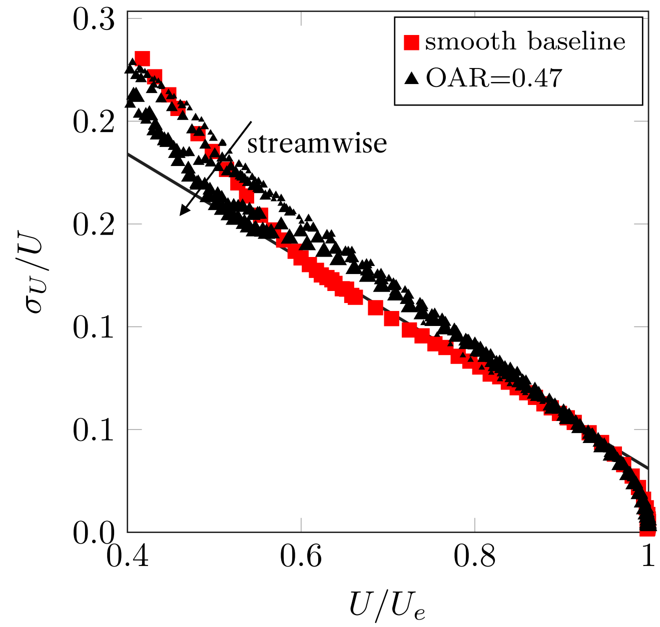

Fig. 5. Diagnostic plot for smooth (red square) and perforated model (black triangle), streamwise evolution for the perforated model, increasing marker size represents more downstream position also indicated by the arrow. Solid line is the relation by Castro et al. (2013) valid for smooth walls. (For interpretation of the references to colour in this figure legend, the reader is referred to the web version of this article.)

Table 1
Boundary layer parameters and friction velocity for the smooth baseline and d6L11 case at 20 m/s. Results obtained 1δ downstream of the last row of cavities using hot wire.

	δ [mm]	Re_τ	Re_θ	H	U_τ (ODI)	U_τ (fit)	l^+ (fit)
Smooth	22.2	1096	3472	1.38	0.77	0.77	61
d6L11	22.9	963	3633	1.45	0.69	0.67	53

increases further downstream, up to above $Y^+ \cong 150$. No plateau was observed within the current measurement domain.

Furthermore, Jaiswal and Ganapathisubramani (2024) observed the formation of an outer peak in the spectrogram at a similar wall-normal location to that of the current investigation. They attributed the outer peak to the formation of very large scale motions (VLSM) on porous surfaces. The wavelength of the outer peak is $\lambda_x^+ \cong 2000$ which corresponds to $\lambda_x/\delta \cong 2$ while (Jaiswal and Ganapathisubramani, 2024) reported a value between 6 and 10. Despite, this difference in wavelength, the outer peak can be bear some similarities with streamwise structures formed over ridge type roughness and is associated with the presence of a secondary flow (Hinze, 1967).

4. Reynolds shear stress decomposition downstream of the perforated region

In Table 1 the boundary layer parameters at the streamwise position of 15δ (1δ downstream of the perforated region, corresponding to the PIV and ODI measurements) are reported for the smooth baseline case and for the d6L11 case at 20 m/s. The values include the friction velocity and the value of the hot wire length in wall units.

The comparison of the statistics between PIV and HWA results for the d6L11 case (OAR = 0.47) is shown in Fig. 9 for the position downstream of the cavities. A good match can be observed between the mean velocity profiles in wall units U^+ (the superscript "+" represents the normalisation by the actual friction velocity) that exhibits deviation from the smooth baseline case evident in the wake region as reported by Scarano et al. (2023a). The PIV results give further confidence in the repeatability of the measurements. What can be highlighted in the Fig. 9(b) is that, as expected, the Reynolds shear stress increases with respect to the baseline case in the region where the outer peak of the standard deviation of the streamwise velocity variance, $\overline{u^2}$, is present. This increase in Reynolds shear stress, $\overline{uv}^+$ and the outer peak formation can directly be linked to the formation of an outer secondary flow structure. Shahzad et al. (2023) and Kuwata and Suga (2016) showed that the inner peak in the streamwise variance decreases for acoustic liners and porous surfaces with respect to smooth walls and scales with the increased porosity. The attenuation of the near wall peak (both in the spectrogram and in the variance) is not documented in the current investigation while a mild increase of the near wall peak with respect to the smooth baseline case is present. This can be a filtering effect attributed to the reduction of the wire length in wall units, l^+, for the perforated condition.

The Reynolds shear stress can be decomposed using the quadrant analysis according to the sign of the velocity fluctuations (Wallace et al., 1972; Wallace, 2016). Q_2 and Q_4 are associated with ejections and sweeps events and contribute to the largest portion of the Reynolds shear stress. The quadrant data can be filtered to consider only the events that contribute significantly to the overall Reynolds shear stress (Nolan et al., 2010). Only the events that are outside a region generated by a set of hyperbolas are considered (also called "hole")

$$|uv| \geq TH_q \quad (1)$$

where the threshold is

$$TH_q = H_q(\sigma_U \cdot \sigma_V) \quad (2)$$

and H_q is a constant. Thus

$$\sum_{i=1}^{4} \overline{uv}_i + \overline{uv}_{H_q} = \overline{uv} \quad (3)$$

where i is the index for the four quadrants.

In Fig. 10 a hole quadrant analysis for the smooth baseline case (red) and the case d6L11 (black) at 20 m/s is reported. The normal-to-wall location analysed is $Y^+ = 200$ and corresponds to the peak of the Reynolds shear stress. Similar results can be obtained from other wall-normal locations where the Reynolds shear stress increases. Fig. 10(a) represents the fraction of each quadrant to the Reynolds shear stress while Fig. 10(b) represents the fraction of duration associated with a given quadrant. In both cases the effect of varying the constant hole size H_q is shown. The duration is only slightly affected by the perforations, but a decrease in the contribution of the sweeps and an increase in the contribution of the ejections to the Reynolds shear stress can be highlighted. The results are almost independent of the threshold values for $1.5 < H_q < 4$ suggesting that the fraction of Reynolds shear stress due to strong ejections increases and the opposite happens for the strong sweeps. For $H_q = 0$ the fraction of ejections does not vary while the fraction of sweeps decreases with respect to the smooth baseline.

The percentage variation of the ejection and sweeps fraction compared to the smooth baseline case for $H_q = 2$ is shown in Fig. 11. The ejection fraction increases with OAR with respect to the smooth baseline case up to a value of about 15% while the sweep fraction decreases by less than 20%. An increase in the intensity of the ejections at the expense of the sweeps would confirm the increased vertical momentum exchange as reported for porous walls (Kim et al., 2020) and as it was suggested from the spectral analysis. According to Kornilov (2015), a predominance of the ejections in the buffer region can be correlated to lower values of wall shear stress while high shear stress is correlated with downward flow due to sweeps. However, as in the current case the quadrant analysis is performed only in the logarithmic region, so it cannot be linked directly with the skin friction reduction. The enhancement of the upward fluid motion in the logarithmic region is compatible with the presence of a secondary flow and the outer

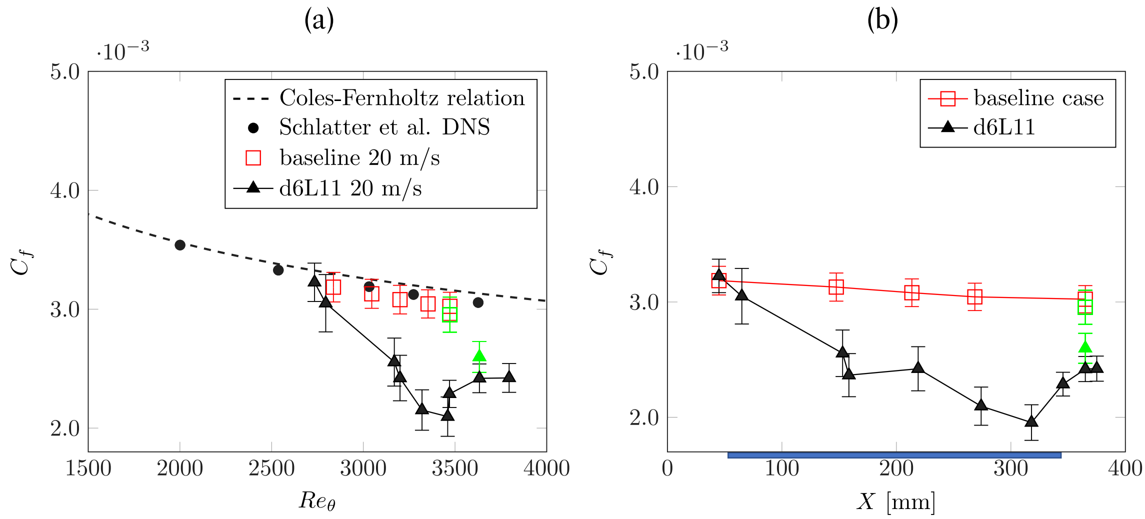

Fig. 6. Streamwise evolution of the friction coefficient obtained with the Clauser's chart technique at 20 m/s, (a) evolution against the local Re_θ, (b) evolution along the model, in blue at the bottom the extension of the perforated region is reported. In green the ODI results for the baseline case (square) and the d6L11 (triangle). (For interpretation of the references to colour in this figure legend, the reader is referred to the web version of this article.)

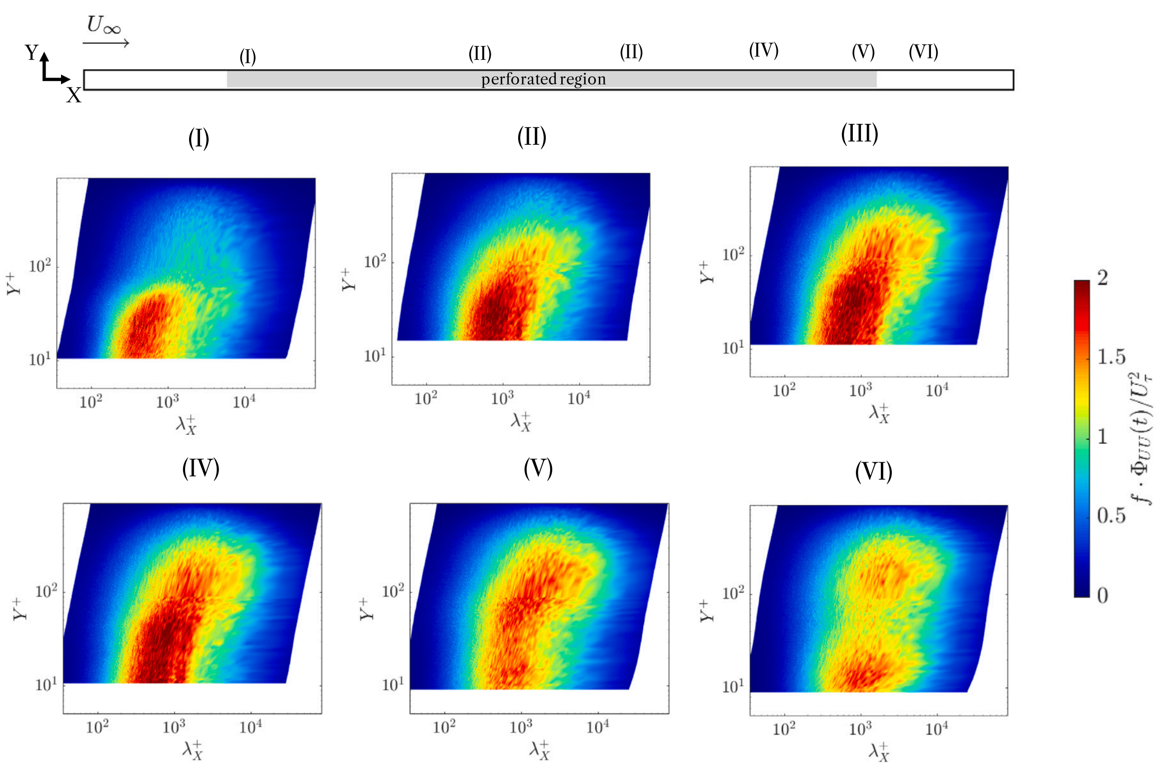

Fig. 7. Streamwise evolution of the contour of the premultiplied energy spectrograms, d6L11 model at 20 m/s; some of the streamwise locations (I) $X = 2.5\delta$, (II) $X = 8\delta$, (III) $X = 10\delta$, (IV) $X = 12.5\delta$, (V) $X = 14\delta$, (VI) $X = 15\delta$.

peak documented in the streamwise evolution of the contours of the premultiplied energy spectrogram. Again there is significant evidence that the secondary flow and the enhanced mixing are promoted for larger OAR.

5. Uniform momentum zones downstream of the perforated region

In turbulent boundary layers, regions known as uniform momentum zones (UMZs) can be identified from PIV snapshots. These zones exhibit consistent streamwise momentum, associated with a modal velocity, U_m, and are directly linked with hairpin vortices and hairpin packets. Details on the procedure to identify the UMZs can be found in Adrian et al. (2000), de Silva et al. (2016), Thavamani et al. (2020) and Scarano et al. (2022a).

For a canonical turbulent boundary layer over a smooth surface (de Silva et al., 2016), as well as for a turbulent boundary layer over riblets and roughness (Heisel et al., 2020) the average number of UMZs is observed to correlate log-linearly with Re_τ. Conversely (Thavamani et al., 2020) reported an increase in $\overline{N}_{\mathrm{UMZ}}$ of about 33%, in presence of an APG along with a similar percentage increase of the boundary layer thickness. The UMZs in the presence of a perforated surface has not

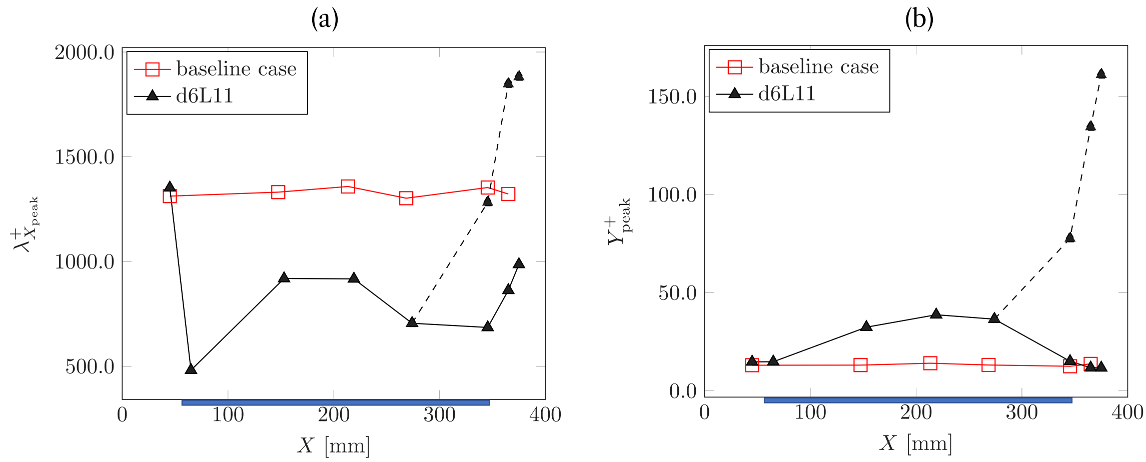

Fig. 8. Streamwise evolution of the spectrum peak at 20 m/s, (a) wavelength, (b) normal-to-wall location. Solid lines represent the inner peak, dashed line represents the outer peak.

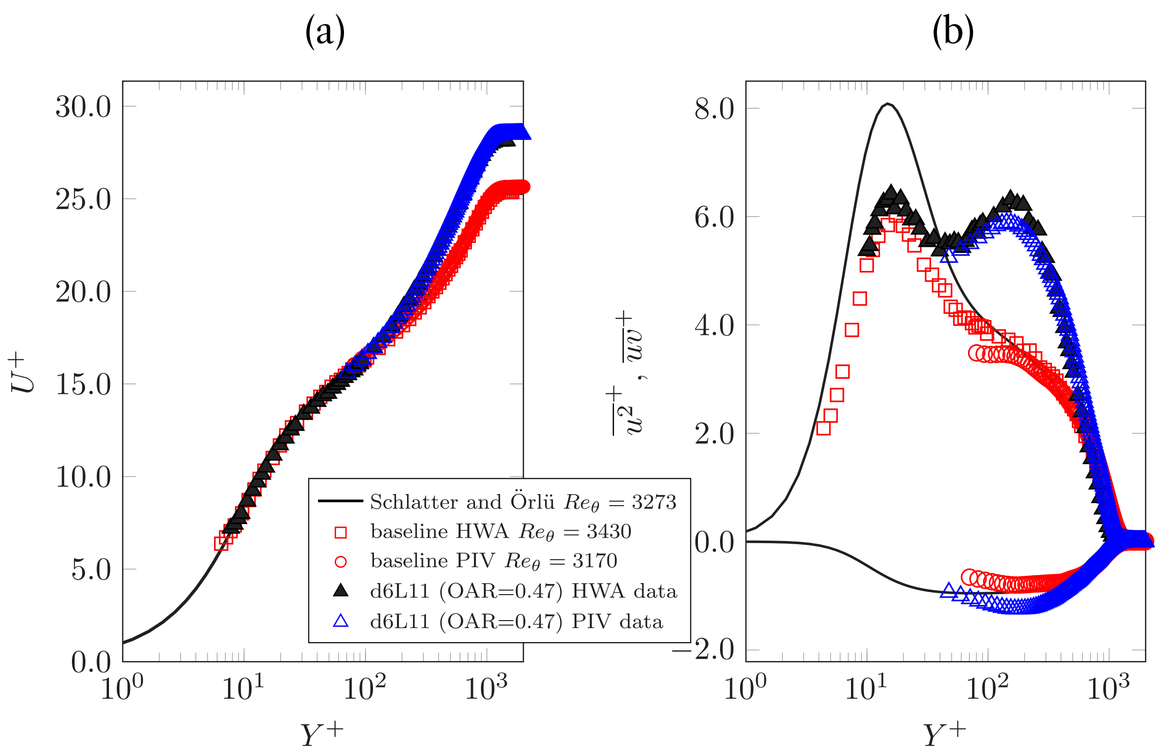

Fig. 9. Mean streamwise velocity, streamwise and Reynolds shear stress in wall units at 20 m/s, actual friction velocity is used (obtained with the method by Rodríguez-López et al. (2015) for HWA data and with ODI for PIV data). Comparison of HWA (black) against PIV data (blue) of the d6L11 case (OAR = 0.47) and baseline case (red). (For interpretation of the references to colour in this figure legend, the reader is referred to the web version of this article.)

been addressed so far and can give further insights on the modification that the turbulent boundary layer undergoes in the presence of circular cavities.

The PDFs of the number of UMZs for the smooth baseline case and for various OAR at 20 m/s are reported in Fig. 12(a); the cavities do not seem to have a significant effect on the PDF of the number of UMZs detected. In Fig. 12(b), the average number of uniform momentum zones, $\overline{N}_{\text{UMZ}}$, is reported for different OAR at the three flow conditions. The number of uniform momentum zones deviates only moderately from the log-linear increase with Re_τ, reported by de Silva et al. (2016). From Fig. 13(a) it can be inferred that the maximum variation of the number of UMZs with respect to the smooth baseline is within 6% and no particular trend with the open area ratio or Reynolds number can be highlighted. This suggests that the variation of the number of uniform momentum zones is not directly linked with the skin friction reduction. Further investigations are needed on this topic. Such an erratic variation of the $\overline{N}_{\text{UMZ}}$, which does not correspond to a Reynolds number (Re_τ) effect, suggests that the influence of the cavities on the hairpin vortices hierarchical arrangement is rather weak and may be linked to the negligible variation of the boundary layer thickness.

The snapshots of the smooth baseline case and d6L11 case at 20 m/s are shown in Fig. 14. The mean separation location and the centroid of a zone are calculated for each snapshot by a streamwise average of the separation locations and the mid point between two separation locations of two adjacent zones. In Fig. 14 the normal-to-wall extension of the zone t_i and the position of the centroid are defined. Each zone can be associated with a value of the average centroid, average thickness

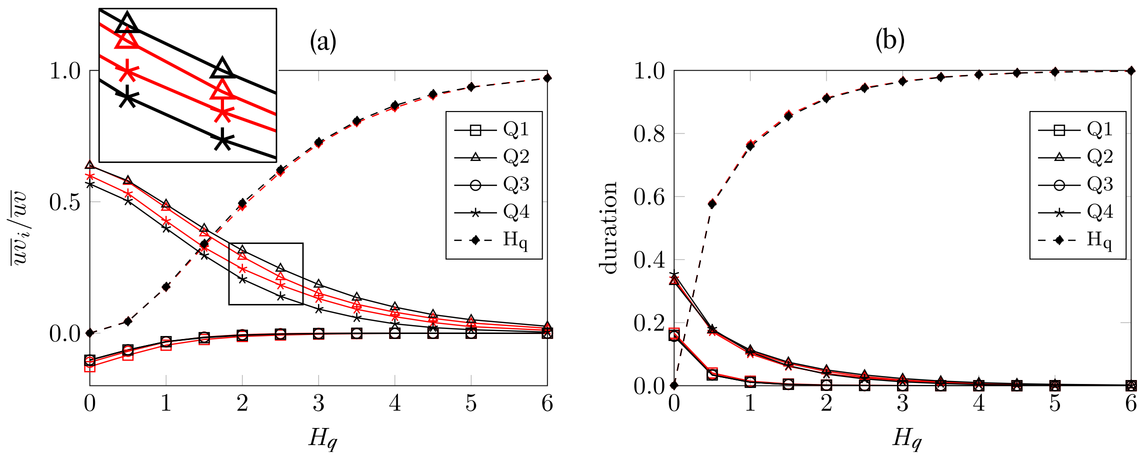

Fig. 10. Quadrant analysis, (a) fraction of the Reynolds shear stress divided into the quadrant events, (b) duration of the quadrant events, in red the smooth baseline, in black d6L11 (OAR = 0.47), $Y^+ \cong 200$, 20 m/s. (For interpretation of the references to colour in this figure legend, the reader is referred to the web version of this article.)

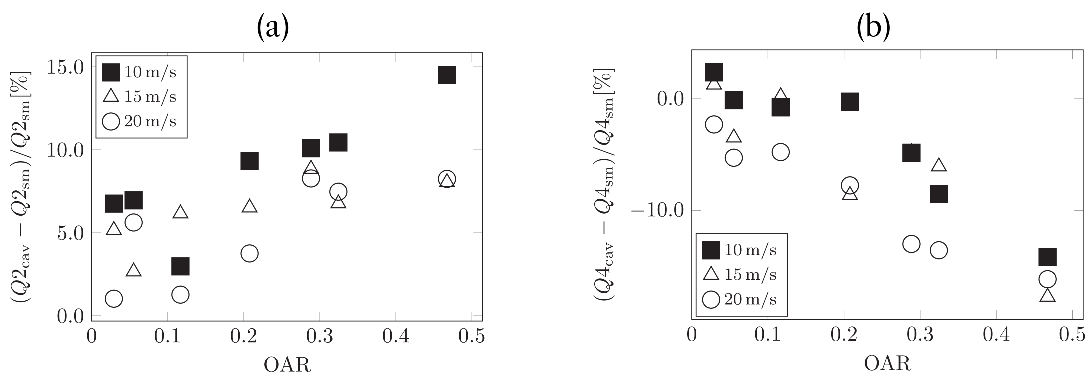

Fig. 11. Quadrant analysis, percentage variation of the fraction of the Reynolds shear stress with OAR (a) ejections Q2, (b) sweeps Q4, $Y^+ \cong 250$, $H_q = 2$.

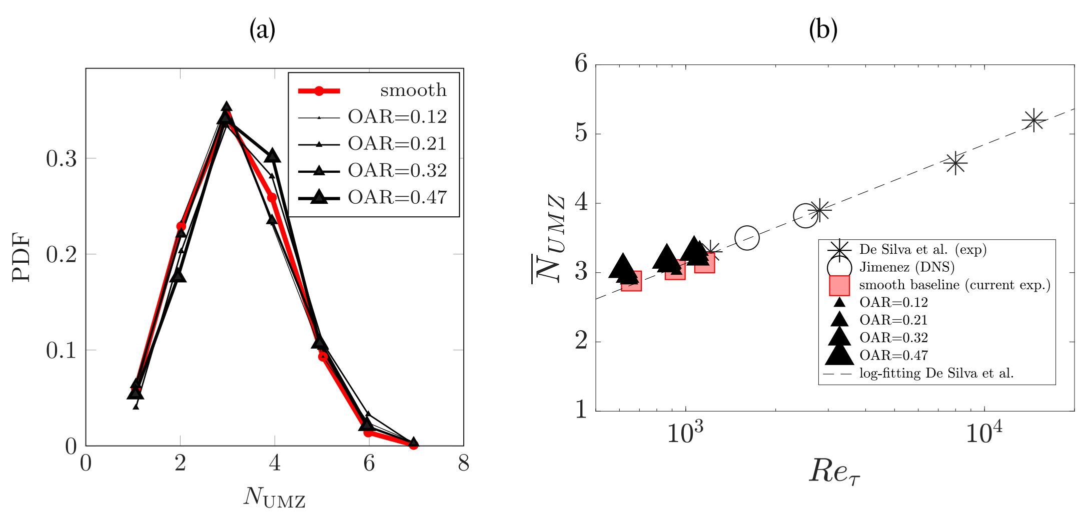

Fig. 12. UMZ for the perforated case, (a) PDF of the number of UMZs detected at 20 m/s, (b) average number of uniform momentum zones detected for the three flow conditions.

and modal velocity

$$Z = f(Y_{\text{centr}}/\delta, U_m/U_\infty, t/\delta). \quad (4)$$

The PDFs of the modal velocities of the zones which have the centroid within a certain range of the boundary layer can be determined and presented in different form. For instance, the PDF of the centroid location is shown in Fig. 15, the three most frequent locations are between 0.1 and 0.2δ, between 0.2 and 0.4δ and between 0.4 and 0.6δ which are used to condition the PDFs (Scarano et al., 2022a).

The PDFs of the overall modal velocities as well as the PDFs of the modal velocity conditioned at a specific location of the centroid are shown in Fig. 16. An overall decrease in the modal velocity can be highlighted from Fig. 16(a) combined with a decrease in the modal velocity of the first zone ($0 < Y_{\text{centr}} < 0.2\delta$) as shown in Fig. 16(b). The decrease in momentum in that normal-to-wall region can be identified

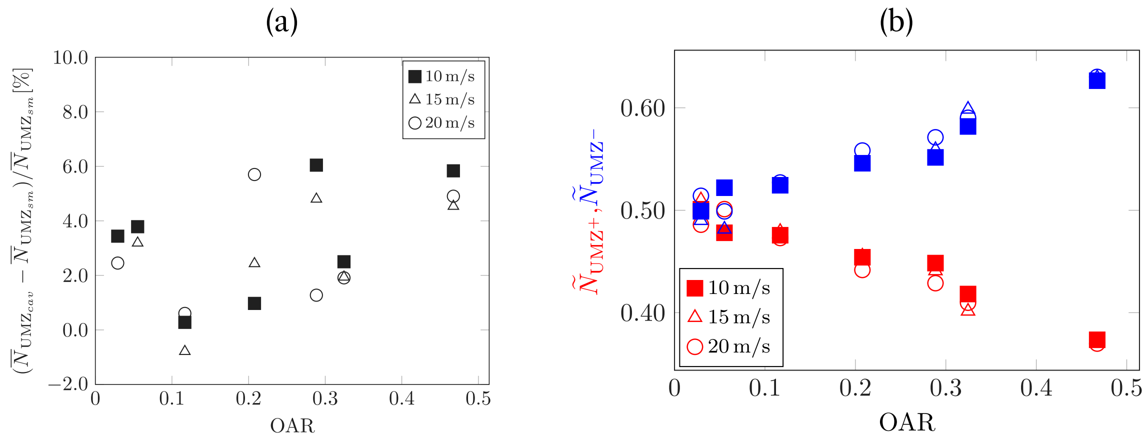

Fig. 13. Percentage variation of the number of UMZs detected with respect to the smooth baseline case (a), fraction of the uniform momentum zones having the modal velocity larger and smaller than the mean velocity of the baseline case at the centre of the interval considered (0–0.2, 0.2–0.4, 0.4–0.6, 0.6–1 Y/δ).

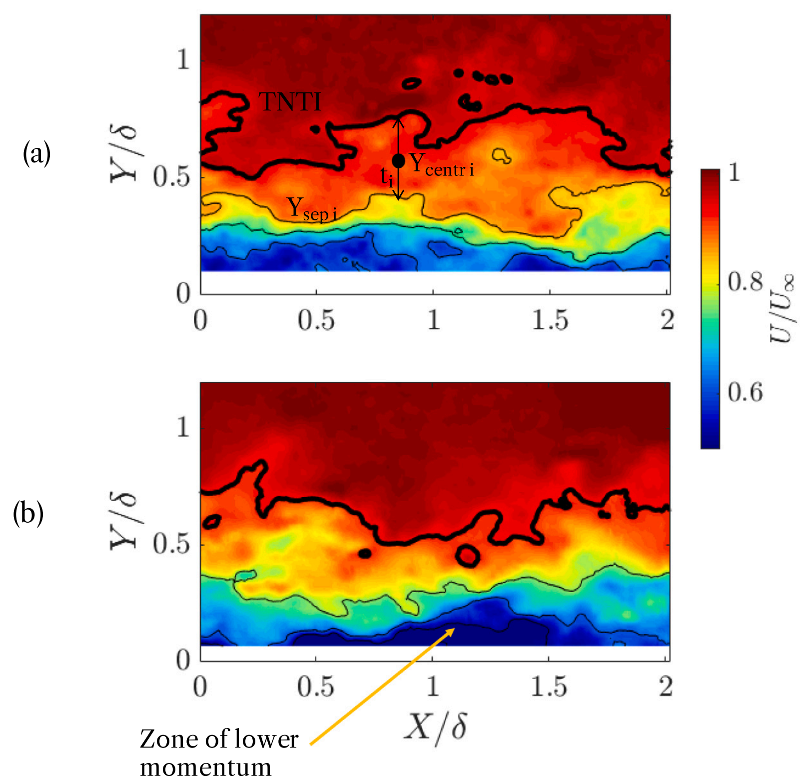

Fig. 14. Randomly chosen PIV snapshots, UMZ detection and parameters definition at 20 m/s, (a) smooth baseline, (b) d6L11 (OAR = 0.47), flow from left to right.

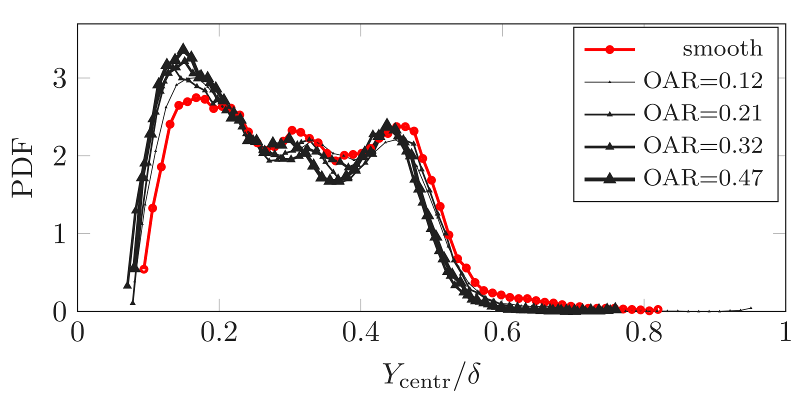

Fig. 15. PDF of centroid location of the UMZs at 20 m/s, markers size represents the increasing OAR.

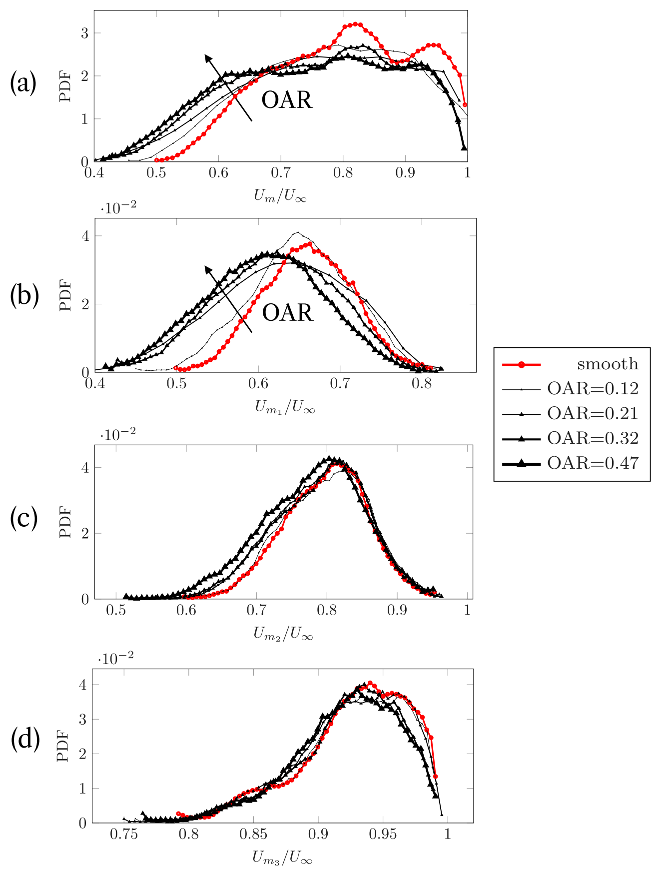

Fig. 16. PDF of modal velocity at 20 m/s, (a) PDF of all the UMZs detected, PDF of the modal velocity for (b) $0 < Y_{\text{centr}} < 0.2$, (c) $0.2 < Y_{\text{centr}} < 0.4$ and (d) $0.4 < Y_{\text{centr}} < 0.6$.

in the randomly chosen snapshot of Fig. 14. For the first zone, a shift in the PDF towards lower values of U_m/U_∞ when the OAR of the perforations increases is easily identifiable. In addition the PDFs are wider, the variance of the modal velocity within a normal-to-wall range increases, which could be linked with the Reynolds shear stress increase. The second region, $0.2\delta < Y_{\text{centr}} < 0.4\delta$, shown in Fig. 16(c) evidences a decrease in the modal velocity compared to the first region. The same trend with respect to the OAR is visible for the second zone but it is less pronounced. The third zone, $0.4\delta < Y_{\text{centr}} < 0.6\delta$, shown in Fig. 16(d) seems to be unaffected by the perforations.

The fraction of the uniform momentum zones having a modal velocity larger or smaller than the mean velocity for the smooth baseline case at the centre of the wall-normal intervals (0–0.2, 0.2–0.4, 0.4–0.6, 0.6–1 Y/δ) is investigated. The criterion is $\widetilde{N}^{+}_{\text{UMZ}}$ if $U_{m_i} > \overline{U}(Y_{c_i})_{\text{smooth}}$ and $\widetilde{N}^{-}_{\text{UMZ}}$ if $U_{m_i} < \overline{U}(Y_{c_i})_{\text{smooth}}$. The results are reported in Fig. 13(b). Despite the overall number of UMZS remains unchanged, the fraction of uniform momentum zones having the modal velocity smaller than the mean velocity of the smooth baseline case increases with the OAR.

The decrease of U_m for increasing OAR indicates that the boundary layer has a lower streamwise momentum in the first zone (which corresponds approximately to the logarithmic layer). This result suggests the formation of a low momentum pathway that is consistent with the formation of large scale outer streamwise structures and would explain the enhanced ejections of low-speed fluid. The effect of the quasi-streamwise structures would then extend up to 0.4δ, while it would be negligible for $Y/\delta > 0.4$.

The modal velocity reduction, associated with the increase in Reynolds shear stress, is a manifestation of the enhanced mixing in the logarithmic region of the boundary layer. As stated by Choi (2002) in the context of spanwise wall oscillations, enhancing the mixing of momentum between the low-speed and the high-speed regions directly influences the skin friction. Such a mixing enhancement can be beneficial for heat transfer purposes as it advects heat from the wall towards the outer region.

6. Summary and concluding remarks

The streamwise characterisation of the boundary layer quantities over the cavity array (d6L11) evidences a negligible variation of the boundary layer thickness with respect to the smooth baseline case and a moderate increase in the shape factor and the momentum thickness. The skin friction decreases with respect to the smooth baseline case starting from right downstream of the first row of cavities and persists even on the smooth portion of the model downstream of the last row of cavities. The skin friction reduction is further confirmed by oil droplet interferometric measurements performed downstream of the perforated region. A qualitative similarity of the current results with uniform blowing by Kametani et al. (2015) is found and this might suggest the presence of an upward fluid motion induced by the perforations. A "two-peak" behaviour is found for the largest perforation condition (d6L11 case) starting from the rear portion of the perforated region. The quadrant analysis showed that in the outer region, the ejection rate increases whereas the sweep rate decreases. These modifications are more pronounced for larger OAR. Negligible differences in the number of uniform momentum zones are found suggesting that the hierarchical arrangement of the hairpin vortices is not modified by the cavities.

The presence of a secondary flow and the formation of outer streamwise structures is potentially responsible for the upward displacement of low momentum fluid from the buffer layer into the logarithmic layer. If on one side the upward momentum transport increases the Reynolds shear stress and the turbulent kinetic energy in the outer region of the boundary layer, on the other side, by supplying low momentum fluid into the logarithmic region, it generates a reduction of the first uniform momentum zone modal velocity. This is translated into a modification of the mean flow and of the mean velocity gradient which in turn can explain the skin friction reduction.

In Scarano et al. (2023a) a similarity between the cavity array and ridge type roughness was reported. The formation of the streamwise vorticity and the secondary flow can in fact be due to the intrinsic surface elevation heterogeneity caused by the cavities that modifies the distribution of Reynolds shear stress gradients (Kadivar et al., 2021). According to the UMZs analysis, the effect of the cavity is confined to the first uniform momentum zone in which the reduced modal velocity suggests the formation of low momentum pathways, here low momentum fluid would be advected into the logarithmic region by streamwise structures. The first uniform momentum zone is indeed located where the contour of the premultiplied energy spectrogram shows the presence of an outer peak that can be linked to a superstructure as those created by the aforementioned imbalance of shear stress in ridge type roughness and documented over porous materials (Shahzad et al., 2023). In addition, the increased contribution of the ejections can be linked with the presence of a secondary flow which, coupled with the upward motion of low momentum, enhances the flow mixing and might play a substantial role in augmenting heat transfer.

As stressed already in Scarano et al. (2023a), the momentum and vorticity flux induced by the perforations would very likely generate a non negligible pressure drag that, as for dimples, can completely overcome the skin friction reduction. Apart from the local drag reduction benefit, the increase in mixing and consequently enhanced heat transfer in the outer part of the boundary layer can play a significant role in passive thermal protection and cooling techniques. Further studies will have to explore a wider range of Reynolds numbers in order to extend the application range of the current setup. The near wall region on top of the cavities should be carefully studied with techniques as μ-PIV and a full direct numerical simulation of the activity inside the cavity is necessary to deeply understand the flow topology and further confirm the hypothesis and conclusions drawn here. Finally, force balance measurements are a fundamental step in order to evaluate the total drag benefit or penalty.

CRediT authorship contribution statement

Francesco Scarano: Writing – review & editing, Writing – original draft, Visualization, Validation, Resources, Methodology, Investigation, Formal analysis, Data curation, Conceptualization. **Marc C. Jacob:** Writing – review & editing, Visualization, Supervision, Project administration, Funding acquisition. **Erwin R. Gowree:** Writing – review & editing, Visualization, Supervision, Resources, Project administration, Funding acquisition.

Declaration of competing interest

The authors have no conflict of interest to declare that are relevant to the content of this article.

Data availability

Data will be made available on request.

Acknowledgements

The research leading to these results received funding from AID (Agence Innovation Défense) under Grant Agreement No 2019 65 0028 for the FriDa project. We are grateful to the "Groupe Technique" at the DAEP and Philippe Barricau for the help in PIV, ODI setup and processing of the images.

The authors have no conflict of interest to declare that are relevant to the content of this article.

References

Adrian, R.J., Meinhart, C.D., Tomkins, C.D., 2000. Vortex organization in the outer region of the turbulent boundary layer. J. Fluid Mech. 422, 1–54. http://dx.doi.org/10.1017/S0022112000001580.

Alfredsson, P.H., Örlü, R., 2018. Large-Eddy breakup devices – a 40 years perspective from a Stockholm horizon. Flow Turbul. Combust. 100 (4), 877–888. http://dx.doi.org/10.1007/s10494-018-9908-4, URL http://link.springer.com/10.1007/s10494-018-9908-4.

Alfredsson, P.H., Segalini, A., Örlü, R., 2011. A new scaling for the streamwise turbulence intensity in wall-bounded turbulent flows and what it tells us about the "outer" peak. Phys. Fluids 23 (4), 041702. http://dx.doi.org/10.1063/1.3581074, URL http://aip.scitation.org/doi/10.1063/1.3581074.

Antonia, R.A., Luxton, R.E., 1971. The response of a turbulent boundary layer to a step change in surface roughness part 1. Smooth to rough. J. Fluid Mech. 48 (4), 721–761. http://dx.doi.org/10.1017/S0022112071001824.

Cafiero, G., Iuso, G., 2022. Drag reduction in a turbulent boundary layer with sinusoidal riblets. Exp. Therm Fluid Sci. 139, 110723. http://dx.doi.org/10.1016/j.expthermflusci.2022.110723, URL https://www.sciencedirect.com/science/article/pii/S0894177722001236.

Castro, I.P., Segalini, A., Alfredsson, P.H., 2013. Outer-layer turbulence intensities in smooth- and rough-wall boundary layers. J. Fluid Mech. 727, 119–131. http://dx.doi.org/10.1017/jfm.2013.252, URL https://www.cambridge.org/core/product/identifier/S0022112013002528/type/journal_article.

Choi, K.-S., 2002. Near-wall structure of turbulent boundary layer with spanwise-wall oscillation. Phys. Fluids 14 (7), 2530–2542. http://dx.doi.org/10.1063/1.1477922, arXiv:https://aip.scitation.org/doi/pdf/10.1063/1.1477922. URL https://aip.scitation.org/doi/abs/10.1063/1.1477922.

de Giovanetti, M., Hwang, Y., Choi, H., 2016. Skin-friction generation by attached eddies in turbulent channel flow. J. Fluid Mech. 808, 511–538. http://dx.doi.org/10.1017/jfm.2016.665.

de Silva, C.M., Hutchins, N., Marusic, I., 2016. Uniform momentum zones in turbulent boundary layers. J. Fluid Mech. 786, 309–331. http://dx.doi.org/10.1017/jfm.2015.672.

Deshpande, R., Chandran, D., Smits, A.J., Marusic, I., 2023. On the relationship between manipulated inter-scale phase and energy-efficient turbulent drag reduction. J. Fluid Mech. 972, A12. http://dx.doi.org/10.1017/jfm.2023.715.

Duvvuri, S., McKeon, B., 2016. Nonlinear interactions isolated through scale synthesis in experimental wall turbulence. Phys. Rev. Fluids 1, 032401. http://dx.doi.org/10.1103/PhysRevFluids.1.032401, URL https://link.aps.org/doi/10.1103/PhysRevFluids.1.032401.

Fukagata, K., Iwamoto, K., Kasagi, N., 2002. Contribution of Reynolds stress distribution to the skin friction in wall-bounded flows. Phys. Fluids 14 (11), L73–L76. http://dx.doi.org/10.1063/1.1516779, arXiv:https://doi.org/10.1063/1.1516779.

Garcia-Mayoral, R., Jimenez, J., 2011. Drag reduction by riblets. Phil. Trans. R. Soc. A 369 (1940), 1412–1427. http://dx.doi.org/10.1098/rsta.2010.0359, arXiv:https://royalsocietypublishing.org/doi/pdf/10.1098/rsta.2010.0359. URL https://royalsocietypublishing.org/doi/abs/10.1098/rsta.2010.0359.

Gomit, G., de Kat, R., Ganapathisubramani, B., 2018. Structure of high and low shear-stress events in a turbulent boundary layer. Phys. Rev. Fluids 3, 014609. http://dx.doi.org/10.1103/PhysRevFluids.3.014609, URL https://link.aps.org/doi/10.1103/PhysRevFluids.3.014609.

Gowree, E., Jagadeesh, C., Atkin, C., 2019. Skin friction drag reduction over staggered three dimensional cavities. Aerosp. Sci. Technol. 84, 520–529.

Gul, M., Ganapathisubramani, B., 2022. Experimental observations on turbulent boundary layers subjected to a step change in surface roughness. J. Fluid Mech. 947, A6. http://dx.doi.org/10.1017/jfm.2022.608, URL https://www.cambridge.org/core/product/identifier/S0022112022006085/type/journal_article.

Heisel, M., de Silva, C.M., Hutchins, N., Marusic, I., Guala, M., 2020. On the mixing length eddies and logarithmic mean velocity profile in wall turbulence. J. Fluid Mech. 887, R1. http://dx.doi.org/10.1017/jfm.2020.23.

Hinze, J.O., 1967. Secondary currents in wall turbulence. Phys. Fluids 10 (9), S122–S125. http://dx.doi.org/10.1063/1.1762429, arXiv:https://aip.scitation.org/doi/pdf/10.1063/1.1762429. URL https://aip.scitation.org/doi/abs/10.1063/1.1762429.

Hwang, Y., 2013. Near-wall turbulent fluctuations in the absence of wide outer motions. J. Fluid Mech. 723, 264–288. http://dx.doi.org/10.1017/jfm.2013.133.

Hwang, D., Biesiadny, T., 1997. Experimental evaluation of penalty associated with micro-blowing for reducing skin friction. In: 36th AIAA Aerospace Sciences Meeting and Exhibit. p. 677.

Ismail, U., Zaki, T.A., Durbin, P.A., 2018. Simulations of rib-roughened rough-to-smooth turbulent channel flows. J. Fluid Mech. 843, 419–449. http://dx.doi.org/10.1017/jfm.2018.119, URL https://www.cambridge.org/core/product/identifier/S0022112018001192/type/journal_article.

Jaiswal, P., Ganapathisubramani, B., 2024. Effects of porous substrates on the structure of turbulent boundary layers. J. Fluid Mech. 980, A39. http://dx.doi.org/10.1017/jfm.2024.45, URL https://www.cambridge.org/core/product/identifier/S0022112024000454/type/journal_article.

Jung, W.J., Mangiavacchi, N., Akhavan, R., 1992. Suppression of turbulence in wall-bounded flows by high-frequency spanwise oscillations. Phys. Fluids A 4 (8), 1605–1607. http://dx.doi.org/10.1063/1.858381, arXiv:https://pubs.aip.org/aip/pof/article-pdf/4/8/1605/12277323/1605_1_online.pdf.

Kadivar, M., Tormey, D., McGranaghan, G., 2021. A review on turbulent flow over rough surfaces: Fundamentals and theories. Int. J. Thermofluids 10, 100077. http://dx.doi.org/10.1016/j.ijft.2021.100077, URL https://www.sciencedirect.com/science/article/pii/S266620272100015X.

Kametani, Y., Fukagata, K., Orlu, R., Schlatter, P., 2015. Effect of uniform blowing/suction in a turbulent boundary layer at moderate Reynolds number. Int. J. Heat Fluid Flow 55, 132–142. http://dx.doi.org/10.1016/j.ijheatfluidflow.2015.05.019, Special Issue devoted to the 10th Int. Symposium on Engineering Turbulence Modelling and Measurements (ETMM10) held in Marbella, Spain on September 17-19, 2014.

Kendall, A., Koochesfahani, M., 2008. A method for estimating wall friction in turbulent wall-bounded flows. Exp. Fluids 44, 773–780. http://dx.doi.org/10.1007/s00348-007-0433-9.

Kim, T., Blois, G., Best, J.L., Christensen, K.T., 2020. Experimental evidence of amplitude modulation in permeable-wall turbulence. J. Fluid Mech. 887, A3. http://dx.doi.org/10.1017/jfm.2019.1027, URL https://www.cambridge.org/core/product/identifier/S0022112019010279/type/journal_article.

Kornilov, V., 2015. Current state and prospects of researches on the control of turbulent boundary layer by air blowing. Prog. Aerosp. Sci. 76, 1–23. http://dx.doi.org/10.1016/j.paerosci.2015.05.001, URL https://www.sciencedirect.com/science/article/pii/S0376042115000329.

Kuwata, Y., Suga, K., 2016. Lattice Boltzmann direct numerical simulation of interface turbulence over porous and rough walls. Int. J. Heat Fluid Flow 61, 145–157. http://dx.doi.org/10.1016/j.ijheatfluidflow.2016.03.006, URL https://www.sciencedirect.com/science/article/pii/S0142727X16300479. SI TSFP9 special issue.

Manes, C., Poggi, D., Ridolfi, L., 2011. Turbulent boundary layers over permeable walls: scaling and near-wall structure. J. Fluid Mech. 687, 141–170. http://dx.doi.org/10.1017/jfm.2011.329.

Mathis, R., Hutchins, N., Marusic, I., 2009. Large-scale amplitude modulation of the small-scale structures in turbulent boundary layers. J. Fluid Mech. 628, 311–337. http://dx.doi.org/10.1017/S0022112009006946.

Naughton, J.W., Robinson, J., Durgesh, V., 2003. Oil-film interferometry measurement of skin friction - analysis summary and description of matlab program. In: 20th International Congress on Instrumentation in Aerospace Simulation Facilities, 2003. ICIASF '03, pp. 169–178.

Naughton, J.W., Sheplak, M., 2002. Modern developments in shear-stress measurement. Prog. Aerosp. Sci. 38 (6), 515–570. http://dx.doi.org/10.1016/S0376-0421(02)00031-3, URL http://www.sciencedirect.com/science/article/pii/S0376042102000313.

Nolan, K.P., Walsh, E.J., McEligot, D.M., 2010. Quadrant analysis of a transitional boundary layer subject to free-stream turbulence. J. Fluid Mech. 658, 310–335. http://dx.doi.org/10.1017/S0022112010001758.

Pailhas, G., Barricau, P., Touvet, Y., Perret, L., 2009. Friction measurement in zero and adverse pressure gradient boundary layer using oil droplet interferometric method. Exp. Fluids 47 (2), 195–207. http://dx.doi.org/10.1007/s00348-009-0650-5, URL http://link.springer.com/10.1007/s00348-009-0650-5.

Patel, V.C., 1965. Calibration of the preston tube and limitations on its use in pressure gradients. J. Fluid Mech. 23 (1), 185–208. http://dx.doi.org/10.1017/S0022112065001301.

Rodríguez-López, E., Bruce, P.J.K., Buxton, O.R.H., 2015. A robust post-processing method to determine skin friction in turbulent boundary layers from the velocity profile. Exp. Fluids 56 (4), 68. http://dx.doi.org/10.1007/s00348-015-1935-5, URL http://link.springer.com/10.1007/s00348-015-1935-5.

Scarano, F., Jacob, M.C., Carbonneau, X., Gowree, E.R., 2022a. On the turbulent boundary layer over a flat plate at moderate Reynolds numbers. Phys. Fluids 34 (11), 115150. http://dx.doi.org/10.1063/5.0124498, URL https://aip.scitation.org/doi/10.1063/5.0124498.

Scarano, F., Jacob, M.C., Gojon, R., Carbonneau, X., Gowree, E.R., 2022b. Modification of a turbulent boundary layer by circular cavities. Phys. Fluids 34 (6), 065134. http://dx.doi.org/10.1063/5.0091110, URL https://aip.scitation.org/doi/10.1063/5.0091110.

Scarano, F., Jacob, M.C., Gowree, E.R., 2023a. Drag reduction by means of an array of staggered circular cavities at moderate Reynolds numbers. Int. J. Heat Fluid Flow 102, 109142. http://dx.doi.org/10.1016/j.ijheatfluidflow.2023.109142, URL https://linkinghub.elsevier.com/retrieve/pii/S0142727X23000413.

Scarano, F., Jaroslawski, T., Gowree, E.R., 2023b. An experimental investigation of turbulent boundary layers over ridge-type roughness with sinusoidal pattern. http://dx.doi.org/10.21203/rs.3.rs-3604086/v1.

Schlatter, P., Orlu, R., 2010. Assessment of direct numerical simulation data of turbulent boundary layers. J. Fluid Mech. 659, 116–126.

Severino, G.F., Silvestri, A., Cazzolato, B.S., Arjomandi, M., 2022. Sensitivity analysis of orifice length of micro-cavity array for the purpose of turbulence attenuation. Exp. Fluids 63 (1), 24. http://dx.doi.org/10.1007/s00348-021-03371-9.

Shahzad, H., Hickel, S., Modesti, D., 2023. Turbulence and added drag over acoustic liners. J. Fluid Mech. 965, A10. http://dx.doi.org/10.1017/jfm.2023.397, URL https://www.cambridge.org/core/product/identifier/S002211202300397X/type/journal_article.

Silvestri, A., Ghanadi, F., Arjomandi, M., Cazzolato, B., Zander, A., 2017. Attenuation of sweep events in a turbulent boundary layer using micro-cavities. Exp. Fluids 58, http://dx.doi.org/10.1007/s00348-017-2345-7.

Spalart, P., Shur, M., Strelets, M., Travin, A., Paschal, K., Wilkinson, S., 2019. Experimental and numerical study of the turbulent boundary layer over shallow dimples. Int. J. Heat Fluid Flow 78, 108438. http://dx.doi.org/10.1016/j.ijheatfluidflow.2019.108438, URL https://linkinghub.elsevier.com/retrieve/pii/S0142727X19302176.

Tay, C., Khoo, B., Chew, Y., 2015. Mechanics of drag reduction by shallow dimples in channel flow. Phys. Fluids 27, 035109. http://dx.doi.org/10.1063/1.4915069.

Thavamani, A., Cuvier, C., Willert, C., Foucaut, J., Atkinson, C., Soria, J., 2020. Characterisation of uniform momentum zones in adverse pressure gradient turbulent boundary layers. Exp. Therm Fluid Sci. 115, 110080. http://dx.doi.org/10.1016/j.expthermflusci.2020.110080, URL https://www.sciencedirect.com/science/article/pii/S0894177719313779.

Titchener, N., Colliss, S., Babinsky, H., 2015. On the calculation of boundary-layer parameters from discrete data. Exp. Fluids 56, 1–18.

van Campenhout, O., van Nesselrooij, M., Lin, Y., Casacuberta, J., van Oudheusden, B., Hickel, S., 2023. Experimental and numerical investigation into the drag performance of dimpled surfaces in a turbulent boundary layer. Int. J. Heat Fluid Flow 100, 109110. http://dx.doi.org/10.1016/j.ijheatfluidflow.2023.109110, URL https://linkinghub.elsevier.com/retrieve/pii/S0142727X23000097.

van Nesselrooij, M., Veldhuis, L.L.M., van Oudheusden, B.W., Schrijer, F.F.J., 2016. Drag reduction by means of dimpled surfaces in turbulent boundary layers. Exp. Fluids 57 (9), 142.

Wallace, J.M., 2016. Quadrant analysis in turbulence research: History and evolution. Annu. Rev. Fluid Mech. 48 (1), 131–158. http://dx.doi.org/10.1146/annurev-fluid-122414-034550, arXiv:https://doi.org/10.1146/annurev-fluid-122414-034550.

Wallace, J.M., Eckelmann, H., Brodkey, R.S., 1972. The wall region in turbulent shear flow. J. Fluid Mech. 54 (1), 39–48. http://dx.doi.org/10.1017/S0022112072000515.